Science
AAAS

Supplementary Materials for

An autonomously swimming biohybrid fish designed with human cardiac biophysics

Keel Yong Lee *et al.*

Corresponding author: Kevin Kit Parker, kkparker@seas.harvard.edu

Science **375**, 639 (2022)
DOI: 10.1126/science.abh0474

The PDF file includes:

Other Supplementary Material for this manuscript includes the following:

Materials and Methods

Human stem cell-derived biohybrid fish fabrication

Fabrication of the tissue-engineered fish (fig. S4) builds upon the processes derived from gelatin-based muscular thin films with modifications (*16, 17*). First, the paper body of biohybrid fish was fabricated. Two pieces of laboratory tape (General-Purpose Laboratory Labeling Tape, VWR, Radnor, PA) were attached together on their adhesive side (fig. S4A). The biohybrid fish outline (fig. S6, A to C) was then laser cut (Model 24, Epilog Laser, Golden, CO) onto the laboratory tape (fig. S4B). Fish body areas where gelatin would be added were also cut out, and placed in 1:1 bleach/deionized water solution for 30 min and in 70% ethanol solution for 30 min to remove any remaining residue.

The laser-cut laboratory tape was placed on the polydimethylsiloxane (PDMS, Sylgard 184, Dow Corning, Midland, MI) stamp with line groove features (25 μm ridge width, 4 μm groove width, and 5 μm groove depth) to make a micropatterned gelatin body parallel to the biohybrid fish's longitudinal axis (fig. S4, C to E). 20% w/v gelatin (Sigma Aldrich, St. Louis, MO) and 8% w/v microbial transglutaminase (MTG, Ajinomoto, Fort Lee, NJ) with phosphate-buffered saline (PBS, Invitrogen, Carlsbad, CA) were warmed to 65°C and 37°C, respectively for 30 minutes. Then, the solutions were mixed to produce a final solution of 10% w/v gelatin and 4% w/v MTG. 500 μl of the gelatin mixture was quickly pipetted onto the inner fish body areas of the laser-cut laboratory tape. Another PDMS stamp with same line groove features was placed on the MTG and gelatin mixture and then a 500 g scale calibration weight was placed on the PDMS stamp to make thin gelatin body. A glass barrier was placed around the samples to prevent fully dry of gelatin. The gelatin portions were cured and crosslinked overnight at room temperature. After the gelatin cured, the weight was carefully removed along with excess gelatin on the sides of the stamp. To minimize damage to the micro-molded gelatin, the coverslip and stamp were immersed in distilled water to re-hydrate the gelatin for an hour. The stamp was then carefully peeled off the gelatin. The resulting paper and gelatin body of biohybrid fish was sterilized in 70% ethanol for 30 min and UV treated for 2 min. Within the custom culturing acrylic chip, the biohybrid fish substrate is rinsed with PBS. An EDC (1-ethyl-3-(3-dimethylaminopropyl)carbodiimide hydrochloride, Thermo Fisher Scientific Inc, MA), N-hydroxysulfosuccinimide (sulfo-NHS, Thermo Fisher Scientific Inc, MA), and fibronectin (FN, BD Biosciences, Sparks, MD) crosslinking to gelatin procedure is then followed. A 10μl of 0.4 mg/ml EDC and a 10μl of 1.1 mg/ml sulfo-NHS in sodium acetate buffer (pH 5.5) solution mixed into a 100μl of 1mg/ml fibronectin. After 15 mins incubation add the entire (120 μl) FN-EDC-NHS solution to 1880 uμl sterile PBS for a final fibronectin concentration of 50 ug/ml. Then add the FN-EDC-NHS solution incubate on the substrate. After 2 hours of incubation with FN-EDC-NHS solution, the same procedure is followed for the other side of the tissue-engineered fish substrate, and incubated in a 37 °C incubator for at least 1 hour (fig. S4F) before the cell seeding.

Commercial human stem cell-derived CMs (human stem cell-derived CMs, Axiogenesis, Ncardia, Belgium) were transduced with Channelrhodopsin-2 (ChR2) and ChrimsonR lentivirus at a multiplicity of infection of 5 for 24 hours. ChR2-expressing human stem cell-derived CMs were seeded onto one side at first (fig. S4G) at a density of 220 k/cm^2. After a day of culture, ChrimsonR-expressing CMs were seeded onto the other side of the biohybrid fish (fig. S4H). The biohybrid fish were released from the excess laboratory tape after 3 days in culture (fig. S4I). Lastly, a plastic floater fin (polymethylpentene film, Sigma Aldrich, St. Louis, MO) was inserted into the tissue-engineered fish (fig. S4J).

Fabrication of Acrylic Chip for muscular bilayer culture and biohybrid fish

The chip was designed within the vector graphics editing software CorelDraw (Corel, Canada). 6.35-millimeter-thick acrylic was then laser cut with a CO_2 laser engraver (VersaLaser 2.0, Universal Laser Systems, Scottsdale, AZ). Half of the cut outs were made to be bottoms of a whole chip by introducing threads into the cut acrylic. The acrylic chips were placed in a 70% ethanol bath along with screws and placed in a sonicator for sterilization and cleaning.

Culture of human stem cell-derived cardiomyocytes (human-CMs)

Human stem cell-derived cardiomyocytes (hSC-CMs) were purchased from Axiogenesis and Ncardia (Leiden, Netherlands) and cultured using the manufacturer's protocols. Briefly, 500 µl of culture media (Ncardia, Leiden, Netherlands) was added to each frozen vial of cells and thawed at 37 °C. Thawed cells were resuspended in 9 mL of complete culture media (Axiogenesis, Ncardia, Leiden, Netherlands) and incubated in a fibronectin (0.01 µg/mL, BD Biosciences, Bedford, MA)-coated T25 flask in a 37 °C incubator for 4 hours, after which puromycin was supplemented to a final concentration of 2 µg/ml. The culture media was replaced with fresh media after an additional 24 hours, and then replaced every 48 hours for cell maintenance until use. For cell seeding on the biohybrid fish, human cardiomyocytes were dissociated with 0.25% trypsin-EDTA (Life Technologies, CA) and resuspended in puromycin free media.

Harvest and culture of neonatal rat ventricular myocyte (NRVMs)

Animal procedures were performed under protocols approved by Harvard University's Institutional Animal Care and Use Committee. Neonatal rat ventricular myocytes (NRVMs) (2-day old) were isolated as previously published (*25*). Briefly, ventricles were removed from 2-day old Sprague Dawley rat pups (Charles River Laboratories, MA). Then, the manually minced tissues were placed in a 0.1% trypsin (Sigma Aldrich, St. Louis, MO) Hanks' Balanced Salt solution (HBSS) solution at 4°C for approximately 14 hours. For additional enzymatic digestion, a 0.1% type II collagenase (Worthington Biochem, NJ) solution at room temperature was used to isolate ventricular myocytes. NRVMs were further dissociated by centrifuging, resuspending with HBSS, and passing the isolated cell solution through a 40 µm cell strainer. The solution was pre-plated twice for 50 minutes each at 37°C in a M199 cell media (Life Technologies) supplemented with 10% heat-inactivated FBS (Life Technologies, CA) to remove fibroblasts and endothelial cells. Resulting NRVMs were seeded onto the biohybrid fish in M199 cell media (Life Technologies, CA) supplemented with 10% heat-inactivated FBS (Life Technologies, CA).

Optogenetics: plasmid constructs and viral transduction

pLenti-Synapsin-hChR2(H134R)-EYFP-WPRE (*19*) and FCK-ChrimsonR-GFP (*20*) was a gift from Karl Deisseroth (Addgene plasmid #20945; http://n2t.net/addgene:20945; RRID:Addgene_20945) and Edward Boyden (Addgene plasmid #59049; http://n2t.net/addgene:59049; RRID:Addgene_59049), respectively. hChR2 and ChrimsonR lentiviral vectors (cTnT-ChR2-eYFP and cTnT-ChrimsonR-mCherry) were constructed by cloning inserts (hChR2(H134R) and ChrimsonR) to lentiviral vectors with a cardiac-specific promotor (the cardiac troponin T, cTnT) and a fluorescent tag (enhanced yellow fluorescent protein, eYFP or red fluorescent protein, mCherry). The lentivirus was produced and purchased

from VectorBuilder Inc (Chicago, IL) and used to infect both human-CMs and NRVMs with lentivirus (5×10^6 TU/ml) per 1 million CMs.

Optical stimulation for independent activation of muscles

Light-emitting diode sources (LED) were used to independently activate ChR2 and ChrimsonR transduced cardiac tissues. Fiber-coupled LED light source (Prizmatix, Israel) at 450nm and 630nm were mounted through mono fiber optic cannulas (flat end, 400 μm diameter, NA 0.48, Doric Lenses Inc, Canada). To change the pacing frequency and duration, each LED source was independently controlled by analog signals that were synthesized with an analog output module (NI 9264, National Instruments, Austin, TX) by a custom software written (*24*) in LabVIEW (National Instruments, Austin, TX), as previously published (*3*). In addition, the analog output module was triggered by digital trigger signals that were generated by two push button switches through a digital board (USB-6501, National Instruments, Austin, TX), allowing the digital signals to change the frequency without time-delay, as previously published (*3*).

Performance measurement and analysis of biohybrid fish

The biohybrid fish was placed in Tyrode's solution (1.8 mM $CaCl_2$, 5 mM glucose, 5 mM Hepes, 1 mM $MgCl_2$, 5.4 mM KCl, 135 mM NaCl, and 0.33 mM NaH_2PO_4 in deionized water, pH 7.4, at 37°C; Sigma Aldrich, St. Louis, MO) in a 22 cm square chamber (VWR International, Radnor, PA) on a hotplate (VWR International, Radnor, PA) and temperature was maintained at 35 ºC to 37 ºC. The recording of swimming performance of biohybrid fish was filmed with a sCMOS camera (Pco.edge, PCO AG, Germany) coupled with a zoom camera lens (Thorlabs Inc, Newton, NJ) at 50 frames per second or a single-lens recorder (AXP55 4K Handycam, Sony, Japan) with a 26.8mm wide-angle lens at 50 frames per second.

For the longevity measurements, the biohybrid fish were detached after 3 days in culture and incubated in complete culture medium (Ncardia, Leiden, Netherlands), allowing them for self-paced swimming. Every one or two weeks, we conducted the performance measurement in a 37ºC Tyrode's physiological salt solution. After each measurement, the biohybrid fish were placed back and incubated in complete culture medium. The culture medium was exchanged with 12 ml of fresh medium for each biohybrid fish every 4 days for cell maintenance.

To check the effect of mechanical signaling on the antagonistic contraction of muscular bilayer tissues, the biohybrid fish were treated with 250 μM streptomycin or 100 μM Gd^{3+} (both from Sigma-Aldrich, St. Louis, MO) before recording, streptomycin or Gd^{3+} for at least 24 hours.

Digital videos recorded during locomotion experiments were converted to image stacks using a custom-made Matlab program (*24*) (R2020b, Mathworks, Natick, MA). The head, body, and tail positions of the biohybrid fish were tracked using an image processing software (ImageJ, NIH, Bethesda, MD). The moving distance of the biohybrid fish was measured during each tail-beat cycle, and the swimming speed was calculated by dividing the cumulative distance travelled by the total time. Tail-beat amplitude was measured as the distance between maximum right and left excursions. Tail-beat angle (θ) was calculated as the body angle difference between chord lines of its anterior body and caudal fin at the maximum right and left excursions. Antagonistic contraction was determined by checking whether a muscle contraction induced the subsequent contraction of the opposite side muscle with any delay or not. The empirical probability of antagonistic contraction was determined by dividing the number of antagonistic contractions by the total number of contractions.

The stress of the muscular bilayer was estimated by considering the geometric relationship of the curvature (κ), radius of curvature (r), length of muscle tissue (l_{muscle}), and tail-beat angle (θ) ($\kappa = 1/r = \theta / l_{muscle}$) (fig. S19) and using a modified Stoney's equation for anisotropic tissue (*3*):

$$\sigma = \frac{E_{gelatin}\, t_{gelatin}^2}{6 t_{muscle}(1-\upsilon_{gelatin}^2)} \kappa = \frac{E_{gelatin}\, t_{gelatin}^2}{6 t_{muscle}(1-\upsilon_{gelatin}^2)} \frac{\theta}{l_{muscle}},$$

where t_{muscle} is thickness of muscle tissue, $t_{gelatin}$ is thickness of gelatin, $E_{gelatin}$ is young's modulus of gelatin and $\upsilon_{gelatin}$ is Poisson's ratio of gelatin (*30*).

Optical mapping of muscle circuit

Calcium activities of the muscle circuit were monitored with a calcium indicator, X-Rhod-1 (Invitrogen, Carlsbad, CA), using a modified tandem-lens macroscope as previously published (*3, 16*). Briefly, our tandem-lens macroscope (Scimedia, Costa Mesa, CA) was equipped with a high-speed camera (MiCAM Ultima, Scimedia, Costa Mesa, CA), a plan APO 1× objective, a collimator (Lumencor, Beaverton, OR) and a 200-mW mercury lamp for epifluorescence illumination (X-Cite exacte, Lumen Dynamics, Canada). A filter set (excitation filter: 580/14 nm, dichroic mirror: 593 nm cut-off, emission filter: 641/75, Semrock, Rochester, NY) was used for X-Rhod-1 imaging.

The biohybrid fish was incubated with 2 μM X-Rhod-1 for 30 min at 37 ºC, rinsed with culture medium with 2% FBS to remove nonspecifically associated dye, and incubated again for 30 mins for complete de-esterification of the dye. Then, the biohybrid fish was rinsed with Tyrode's solution and mounted on a 37 ºC heating stage (Warner Instruments, Hamden, CT) of the tandem-lens macroscope.

Post-processing of the raw calcium data was conducted with custom software written in MATLAB (*24*) (R2020b, MathWorks, Natick, MA). A spatial filter with 3 × 3 pixels was applied to improve the signal-noise ratio. Activation time of each pixel was calculated at the average maximum upstroke slope of multiple pulses of X-Rhod-1 signals over a 5 second recording window. The total activation time was determined as the difference between activation times at the last and the first activation sites along the posterior body of biohybrid fish.

Particle imaging velocimetry of biohybrid and animal fishes

Flow fields generated by the biohybrid and animal fish were monitored using Particle imaging velocimetry (PIV).

For the PIV measurement of biohybrid fish, we seeded algae particles (10-12 μm diameter, *Tetraselmis sp.*, Reed Mariculture) in Tyrode's solution in a water chamber. 450nm and 630nm LED sources were used to independently activate ChR2 and ChrimsonR transduced cardiac tissues through mono fiber optic cannulas (flat end, 400 μm diameter, NA 0.48, Doric Lenses Inc, Canada). While infrared LED sources (IR30, CMVision, Houston, TX) illuminated the particles, the motions of the particles were recorded at 100 frames per second with a sCMOS camera (Pco.edge, PCO AG, Germany).

For the PIV measurement of freely-swimming animal fish, we placed individual larval zebrafish, white molly, and *Micro-devario kubotai* in a recirculating flow tank at speeds of 1.5 to 3.2 body lengths per second (not including zebrafish: for zebrafish, we did not circulate flow). While infrared LED sources (IR30, CMVision, Houston, TX) illuminated seeded algae particles, the motions of the particles were recorded at 250-500 frames per second with a high-speed video camera (Photron PCI-2014, San Diego, CA).

Flow patterns of both biohybrid and animal fish were analyzed by calculating the velocity distribution within seeded particles between successive video frames using an open-source software (PIVlab 2.02 (*46*)) written in MATLAB (R2014b, MathWorks, Natick, MA).

Immunofluorescent staining and imaging of biohybrid fish

Biohybrid fish was fixed for 12 min in 4% paraformaldehyde (Electron Microscopy Sciences, Hatfield, PA) and 0.5% Triton-X (Sigma-Aldrich, St. Louis, MO) in PBS at 37 °C and incubated with mouse anti-sarcomeric α-actinin monoclonal primary antibody (Sigma-Aldrich, St. Louis, MO), and then stained with DAPI (Sigma-Aldrich) and goat anti-mouse secondary antibody conjugated to Alexa-647 (Invitrogen, Carlsbad, CA). The biohybrid were mounted on glass slides with ProLong Gold antifade mountant (Invitrogen, Carlsbad, CA). All images of biohybrid fish were acquired with an inverted microscope (Olympus IX83, Tokyo, Japan) with an attached spinning disk confocal system (Andor, Concord, MA), and three-dimensional reconstructions of images of muscular bilayer were analyzed and processed using image-processing software (ImageJ 1.52p, NIH, Bethesda, MD).

Muscle mass measurement of biohybrid fish

The muscle mass of 42-days old biohybrid fish was measured by a laboratory scale (Mettler Toledo, Columbus, OH). The muscle mass was measured by subtracting the mass of gelatin-paper substrate (without cell seeding) from the total mass of biohybrid fish. In another way, we estimated the muscle mass of biohybrid fish using the single cell mass and the number of seeded cardiomyocytes on the gelatin portions. To estimate the mass of single cardiomyocyte, the mass of two million of cardiomyocytes was measured and then divided by the number of cardiomyocytes.

Local source-sink mismatch in various corner designs

In cardiomyocytes, pacemaking arises from an interplay between hyperpolarizing and dominating depolarizing currents during the phase 4 depolarization period (the period between repolarization and the rising phase of the subsequent action potential). In the sinoatrial node, the hyperpolarization-induced inward current (HCN isoforms) of cardiac pacemaker cells plays a major role in pacemaking (*47*). However, in the case of our G-node where stem cell-derived CMs and NRVMs supposedly lack the expression of HCNs, the pacemaking potentials are a result of inward currents produced by Ca^{2+} cycling (driven by rhythmic releases of intracellular Ca^{2+} from the sarco/endoplasmic reticulum) (*48*).

The remaining question was how a region of cells initiate coordinated pacemaking and how this relates to electrical cell-to-cell coupling. The geometrical node design plays a crucial role here because the current being exchanged between individual cells of different membrane potentials is locally accumulated in the membrane capacitance at the edges and is reflected at the tissue edges (*12, 23*). The reflection of intracellular currents at the tissue edges synchronizes the spontaneous activity in the structurally isolated small tissues like a G-node and increases their firing rate. The mechanism of reflection at the corners of cultures behave similarly (since downstream impedance is reduced), in particular the anterior corners with acute angles albeit less than in the G-node, and as a result, firing is enhanced in the whole anterior side (Anterior ventral corner: AV, Anterior dorsal corner: AD, and G-node).

To test the theoretical considerations, we investigated the role of geometric factors of the G-node and sink that determine the leading muscle activation site in human stem cell-derived cardiomyocyte tissue (fig. S14 and S15, and movie S14).

1) G-node integration: G-node integrated tissues predominantly activated the muscle construct at the G-node compared to the four corners of the muscle tissue (G-node: 72% vs corners: 5-9% in fig. S14A).

2) Sink's corner design: Rounding the sink's corners decreased the corners' activation probability, thus increasing the probability of activation at the G-node activation to 91% (A3 in fig. S14).

3) G-node's corner design: To investigate the contribution of a sharp corner to the probability of initial activation at the G-node, we compared square and diamond G-nodes to our circular G-node design. The square and diamond G-nodes (B2 and B3 in fig. S14) have a similar probability of activation at the G-node to the circular design (83 and 87% vs. 91%), which indicates that acute angles in a small source tissue like the G-node is not critical in determining the activation site. Rather, the effect of the borders of the small G-node to enhance the electrical interaction between the cells (through so-called reflection of electrotonic current) produces a relatively fast and synchronized activation (*12, 23*).

We conducted quantitative analysis to define the role of reflection boundaries (linear border, edges of different shapes, and the absence of a border) in tissue activation. We also provided a fitting function (fig. S15) for guiding future G-node designs.

The method to quantify the contribution of the corner designs to the probability of initial activation was added in Materials and Methods. Briefly, we estimated the number of downstream cells to be activated by a spontaneously activated cell at a given corner. Given that cells in a corner compete with cells at the G-node to initiate activation waves, we introduced a variable ζ, comparing the two probabilities of initial activation at the corner (P) and at the G-node ($P_{G\text{-}node}$),

$\zeta = P/P_{G\text{-}node}$.

We calculated the ζ of various G-node-integrated tissue designs and compared the number of downstream cells to the ζ of various designs.

As we hypothesized in "Theoretical considerations", the efficacy of the source to initiate activation, ζ, increases with the decreased number of downstream cells (fig. S15). This analysis result underline the source-sink mismatch principle that affects the muscle activation site.

Histology of animal fish

All animal procedures were done in accordance with the guidelines of Harvard University's Animal Care and Use Committee. Fishes were anesthetized in neutrally buffered MS222. Fish were either bred in lab or purchased from Uncle Ned's Fish Factory (Millis, MA).

Tissue samples of fishes were washed by PBS and then fixed in 4% Paraformaldehyde (SigmaAldrich, St. Louis, MO), which were incubated at 4ºC for 24 hours. The samples were decalcificated with Decalcifier-Original (Avantik, Pine Brook, NJ) for 2.5 h and incubated with 5% sodium sulfate solution for 12 h. Decalcification, paraffin embedding, sectioning, imaging, and staining with Masson Trichrome stain were completed by Applied Pathology Systems (Shrewbury, MA).

Statistical analysis

Statistical analysis was performed using JMP Pro 15 (SAS Institute, Inc.). Functional performances of the biohybrid fish were compared using one-way ANOVA followed by Tukey-

Kramer honestly significant difference test. Data represent mean ± SEM. The numbers of fish indicate the numbers of independent experiments.

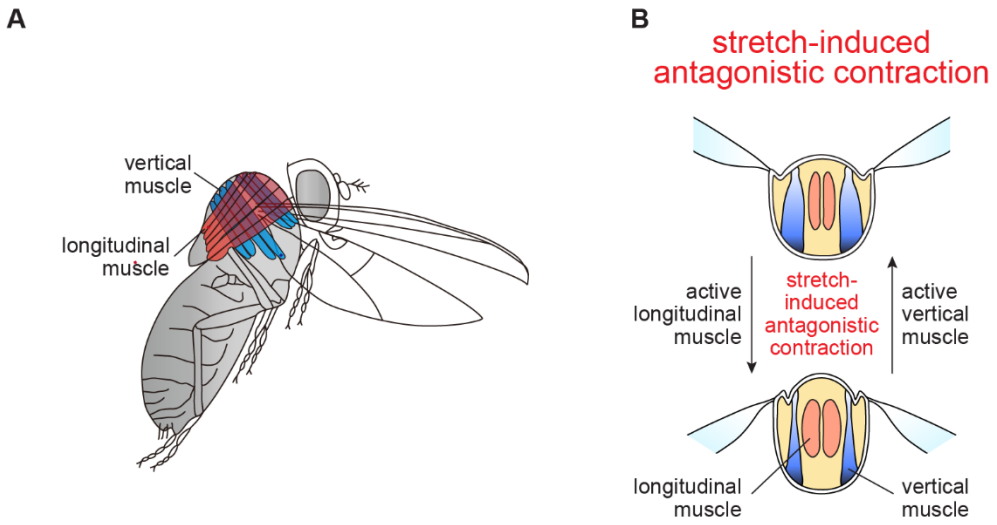

Fig. S1.

Insects' asynchronous muscle contractions. (A) Asynchronous muscle pair (vertical and longitudinal muscles) is arranged perpendicular to each other. **(B)** Each contraction results automatically as a response to the stretching of an antagonistic muscle pair, generating self-sustained muscle contraction cycles.

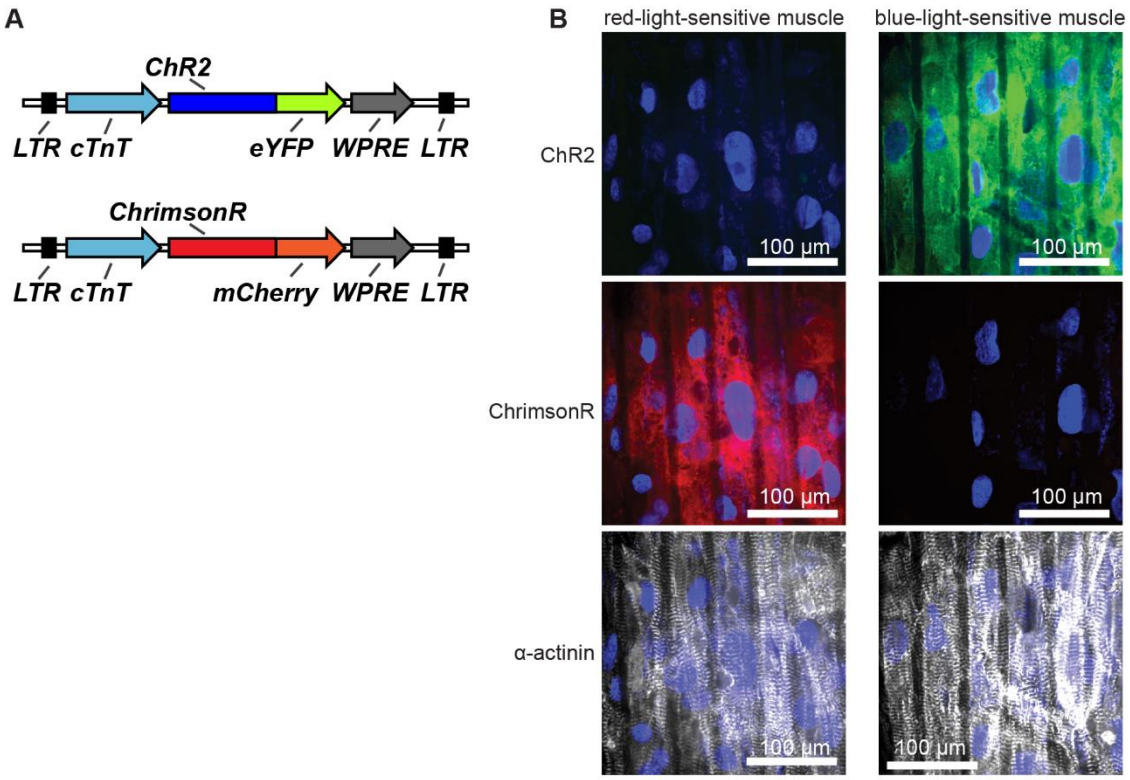

Fig. S2.

Optogenetic cardiac tissue engineering. (A) Construct design of lentiviral vector for cardiac-specific transduction of channelrhodopsin-2 (ChR2) and ChrimsonR. The lentiviral vectors for ChR2 and ChrimsonR transduction were constructed with a cardiac-specific promotor, cTnT promoter, and a fluorescence tag, eGYP or mCherry. **(B)** Immunofluorescence images show that ChR2 and ChrimsonR were mutually exclusively expressed in each muscle layers (representative of n = 10 recorded images). The muscular structure of muscular bilayer was aligned along the longitudinal direction of the micro-mold gelatin substrate.

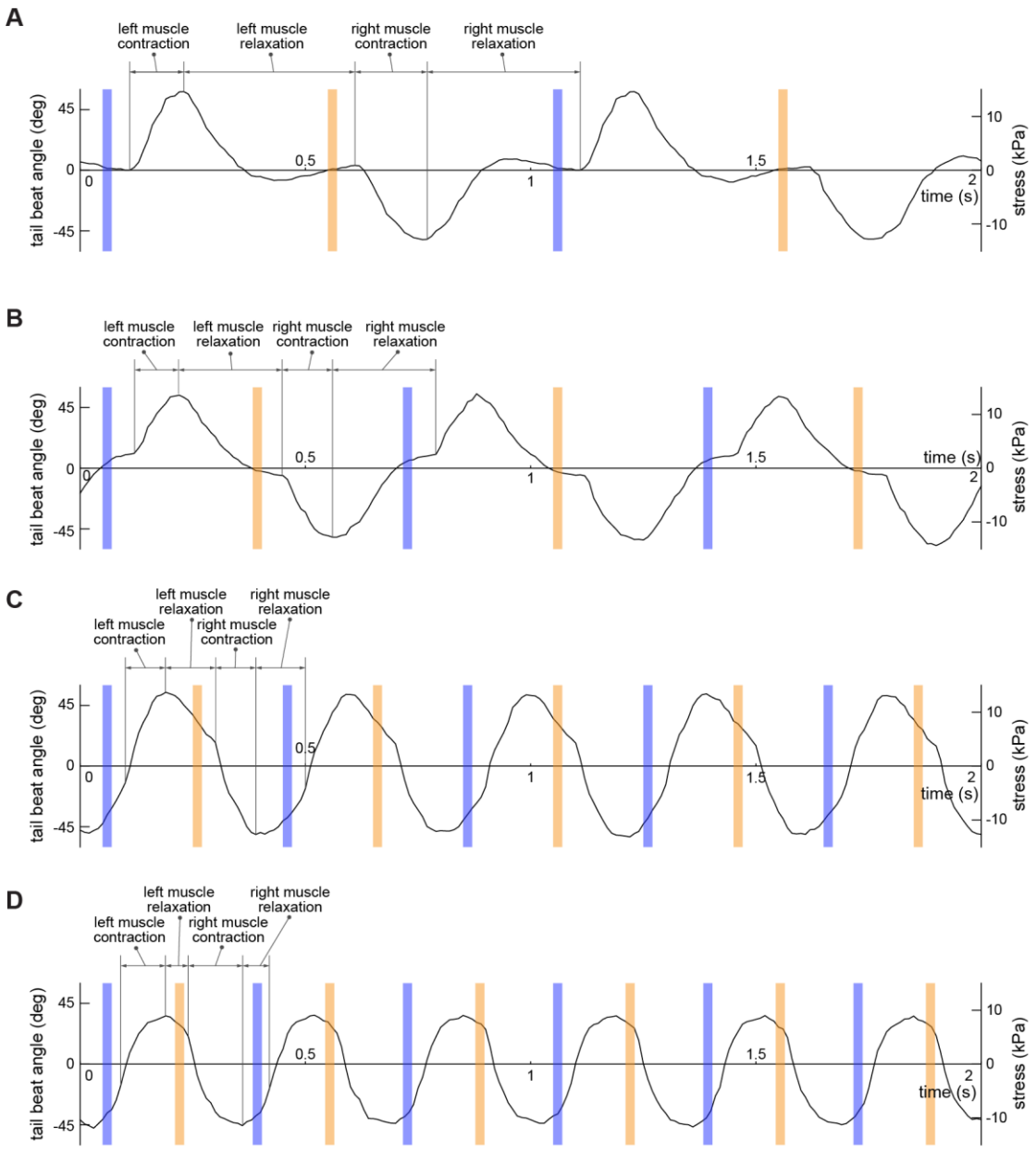

Fig. S3.

Optogenetic control for muscular bilayer cantilever construct at a wide pacing range: (A) 1 Hz, (B) 1.5 Hz, (C) 2.5 Hz, and (D) 3 Hz. Blue and red light independently activate ChR2- and ChrimsonR- expressed muscle layer, respectively. At low pacing frequencies (1 and 1.5 Hz), the contraction and relaxation between one side muscle and the other side muscle are fully decoupled. Thus, the relaxation of each muscle layer causes the muscular bilayer cantilever to recover from the maximum bending to the near-straight position. But, as pacing frequencies increase (2.5 and 3 Hz), the relaxation of one side muscle gets overlapped with the consecutive contraction of the other side muscle. Thus, the consecutive muscle contraction dramatically increases the recovering speed of muscular bilayer tissue at the near-straight position. Data are representative of three muscular bilayer tissues.

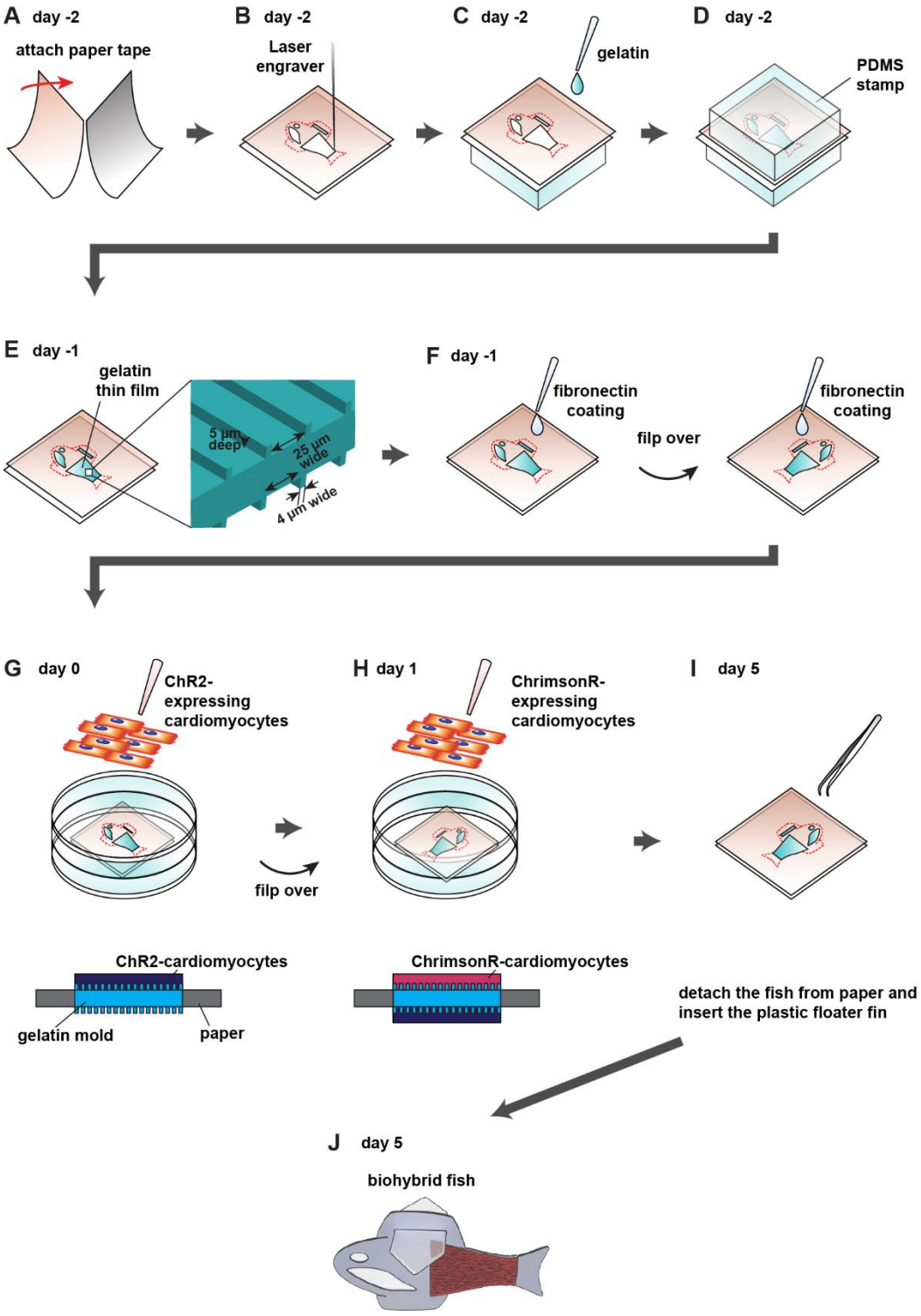

Fig. S4.

Fabrication process for biohybrid fish. (A) Two pieces of painter's tape were attached together on their adhesive side. **(B)** The biohybrid fish outline was then laser cut onto the painter's tape. **(C** to **E)** A MTG and gelatin mixture was sandwiched between two PDMS stamps with line

groove features to make a micropatterned gelatin body parallel to the biohybrid fish's longitudinal axis (C and D). The gelatin portions were cured and crosslinked overnight, then detached from the PDMS stamps (E). **(F)** Both sides of gelatin portions were coated with fibronectin. **(G** and **H)** ChR2-expressing human stem cell-derived CMs were seeded onto one side at first (G), and after a day of culture, ChrimsonR-expressing CMs were seeded onto the other side (H). **(I)** The Biohybrid fish were released from the excess painter's tape after 3 days in culture. **(J)** Lastly, a plastic floater fin was inserted into the tissue-engineered fish.

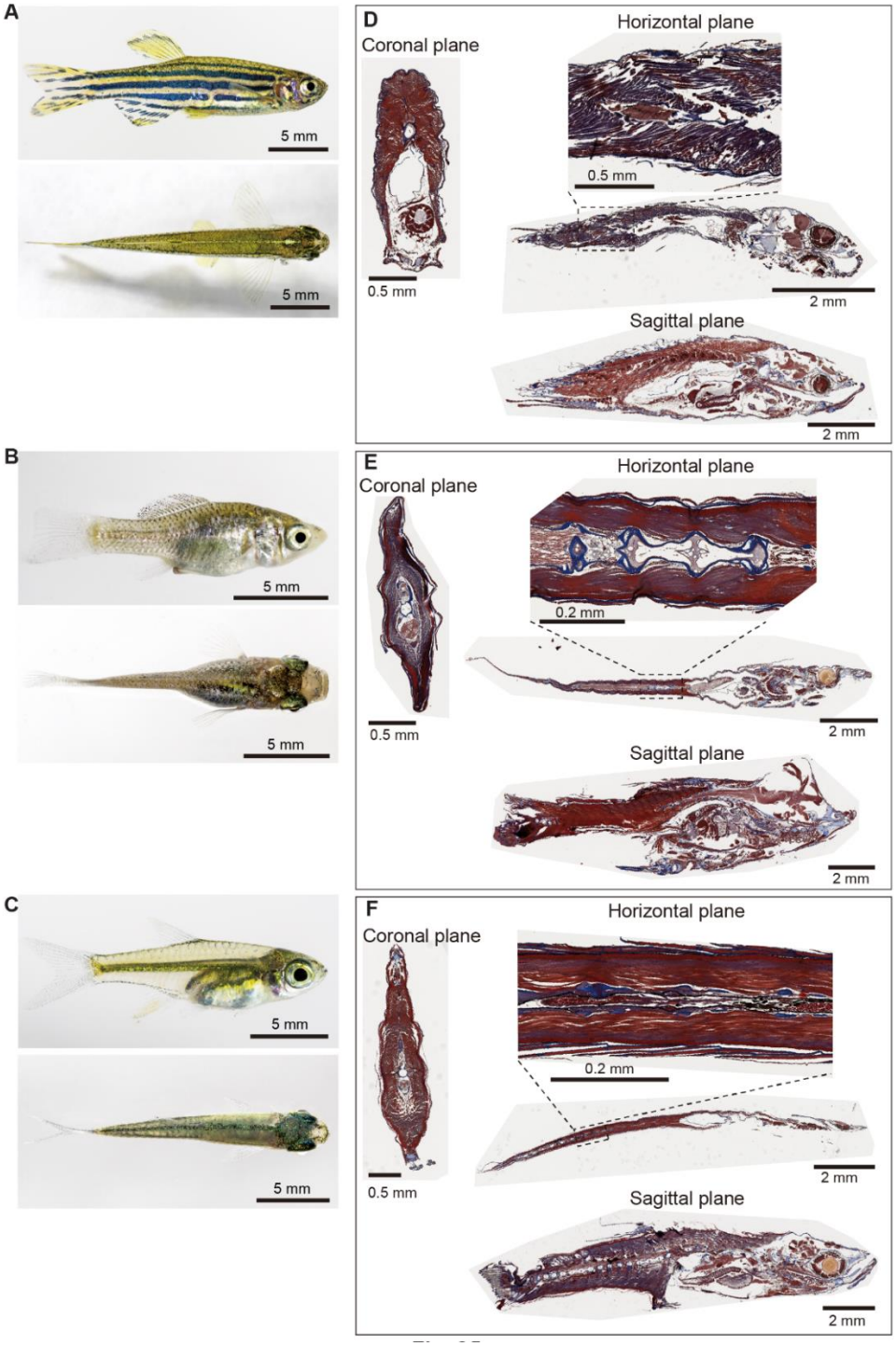

Fig. S5.

Muscular structure of wild-type swimmers. (A) Live larval zebrafish, **(B)** white molly, and **(C)** *Micro-devario kubotai* and **(D** to **F)** their histological coronal, horizontal, and sagittal cross sections. Sections were stained with Mallory's trichrome: red and blue indicates muscle tissue and collagen, respectively. Images are representative of three biologically independent samples per species.

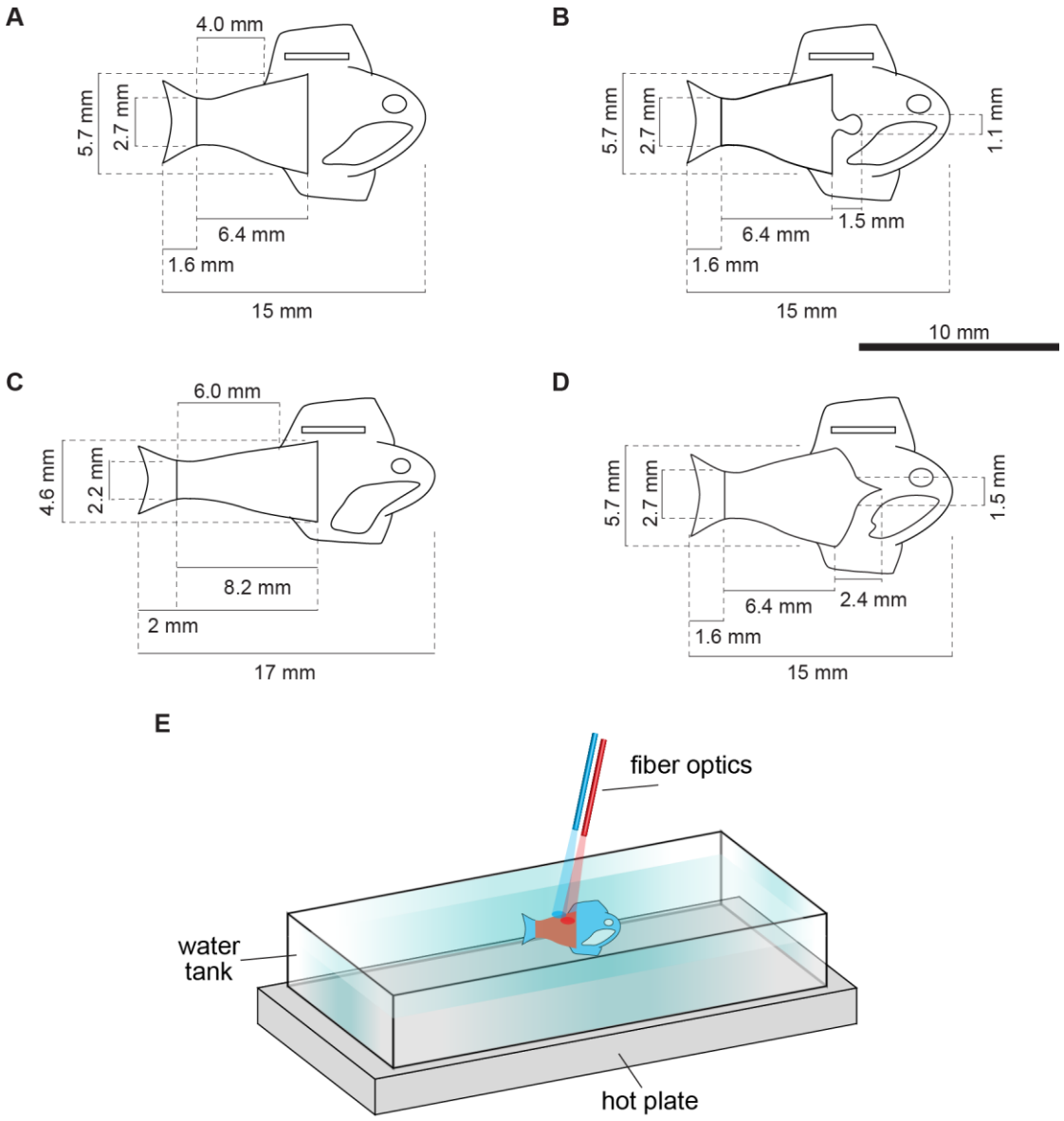

Fig. S6.

Design of biohybrid fish (A) without G-node, **(B)** with G-node, (**C**) with long body length and (**D**) with small point node design G-node and **(E)** experimental setup.

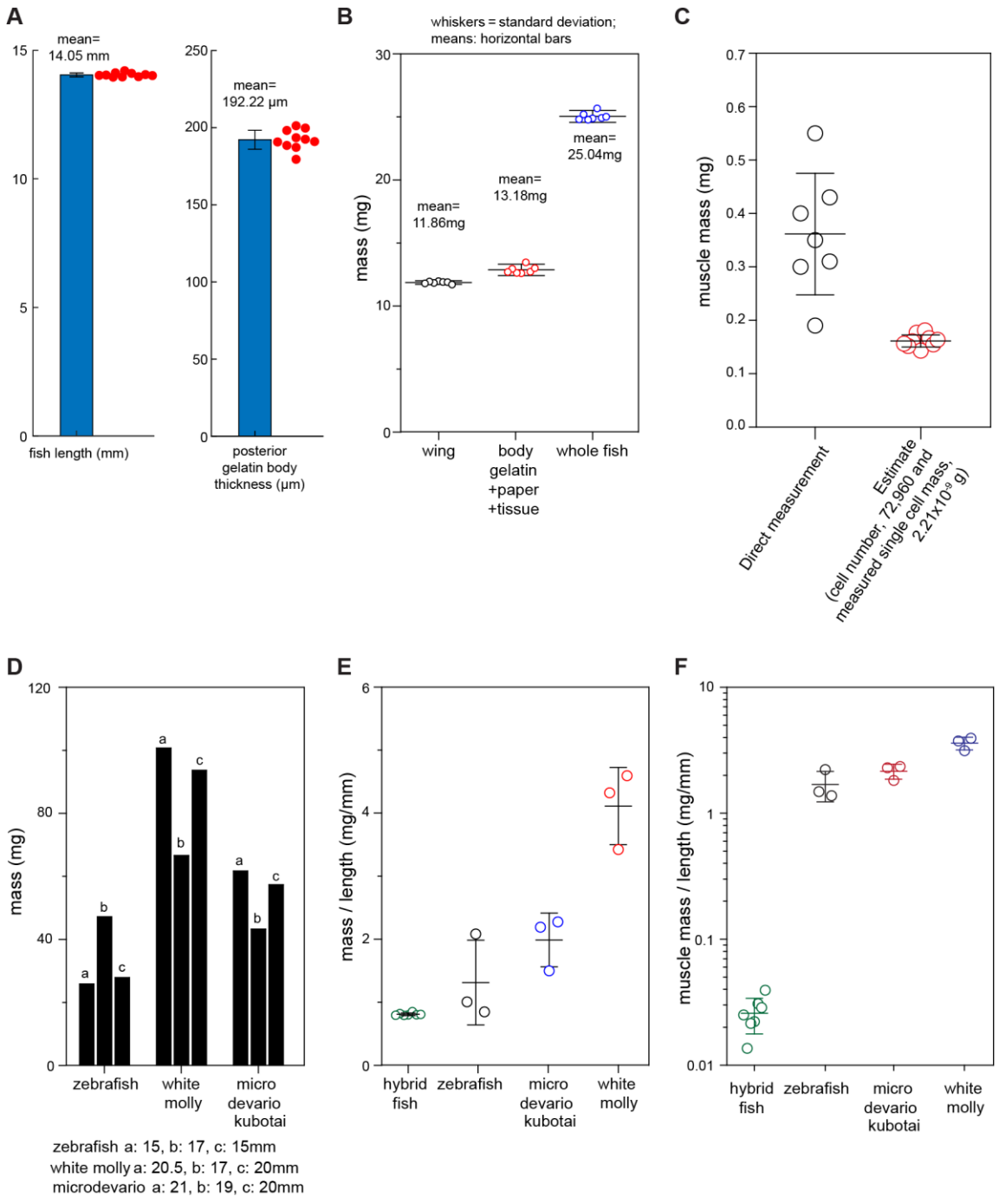

Fig. S7.

Body length and mass of biohybrid and wild-type fish. (A) Length and thickness of posterior gelatin body (n = 10 biohybrid fish; data represent mean ± SD). **(B)** Mass composition of biohybrid fish. **(C)** Muscle mass of biohybrid fish. **(D)** Mass of live larval zebrafish, white molly, and *Micro-devario kubotai*. **(E)** Comparison of ratios of mass to body length between biohybrid and wild-type fish. **(F)** Comparison of ratios of muscle mass to body length between biohybrid and wild-type fish. (n = 7 biohybrid fish, n = 3 wild-type fish; data represent mean ± SD).

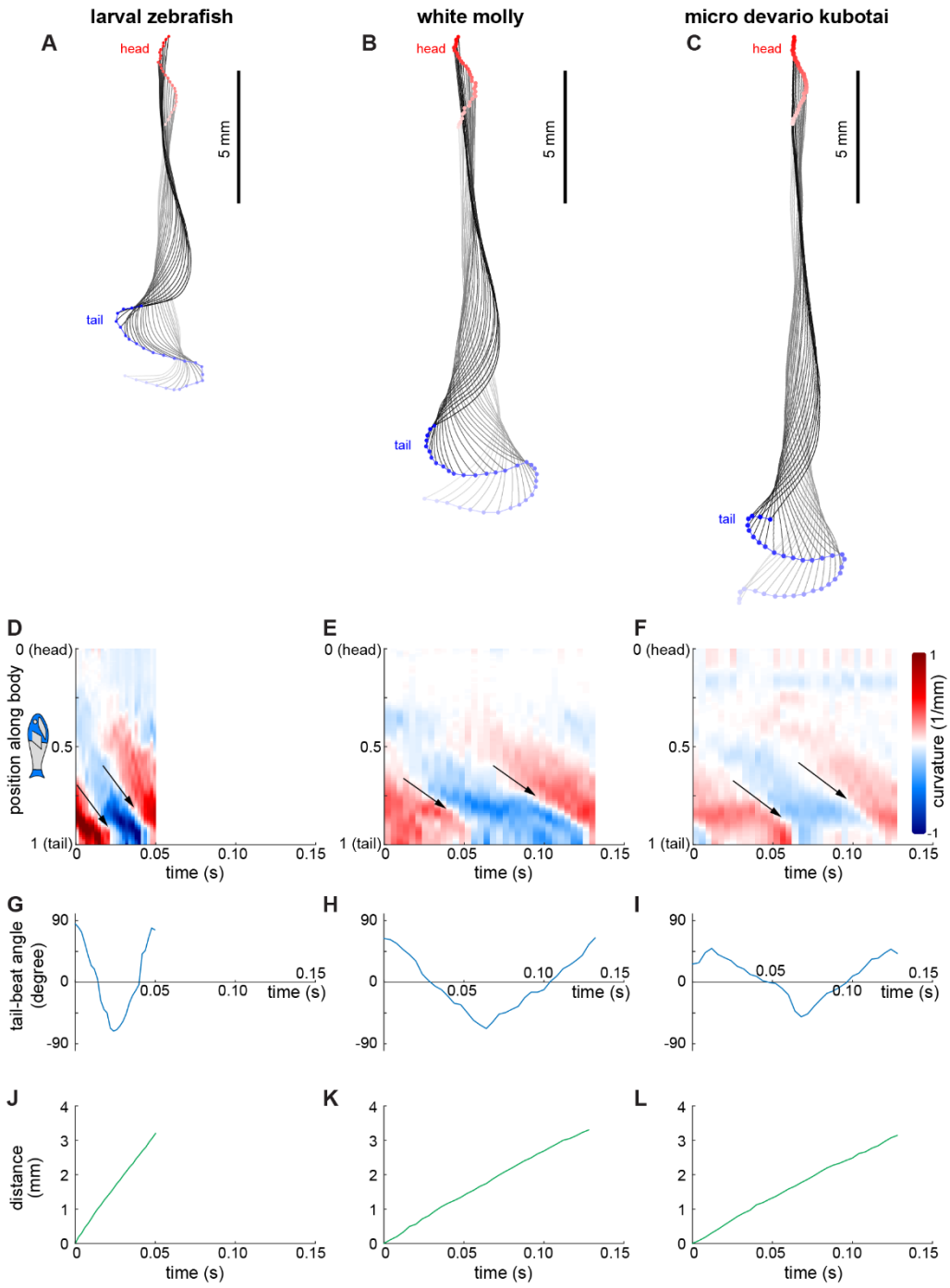

Fig. S8.

Body kinematics of wild-type swimmers during single left and right muscle stroke. (A to **C)** Midline kinematics. **(D** to **F)** Curvature of the midline. **(G** to **I)** Tail beat angle. **(J** to **L)** Moving distance. Live larval zebrafish (A, D, G, and J: body length, l_b: 12 mm, movie S4), white molly (B, E, H, and K, l_b: 19 mm, movie S5), and *Micro-devario kubotai* (C, F, I, and L, l_b: 20 mm, movie S6) have comparable body length of biohybrid fish (l_b: 14 mm).

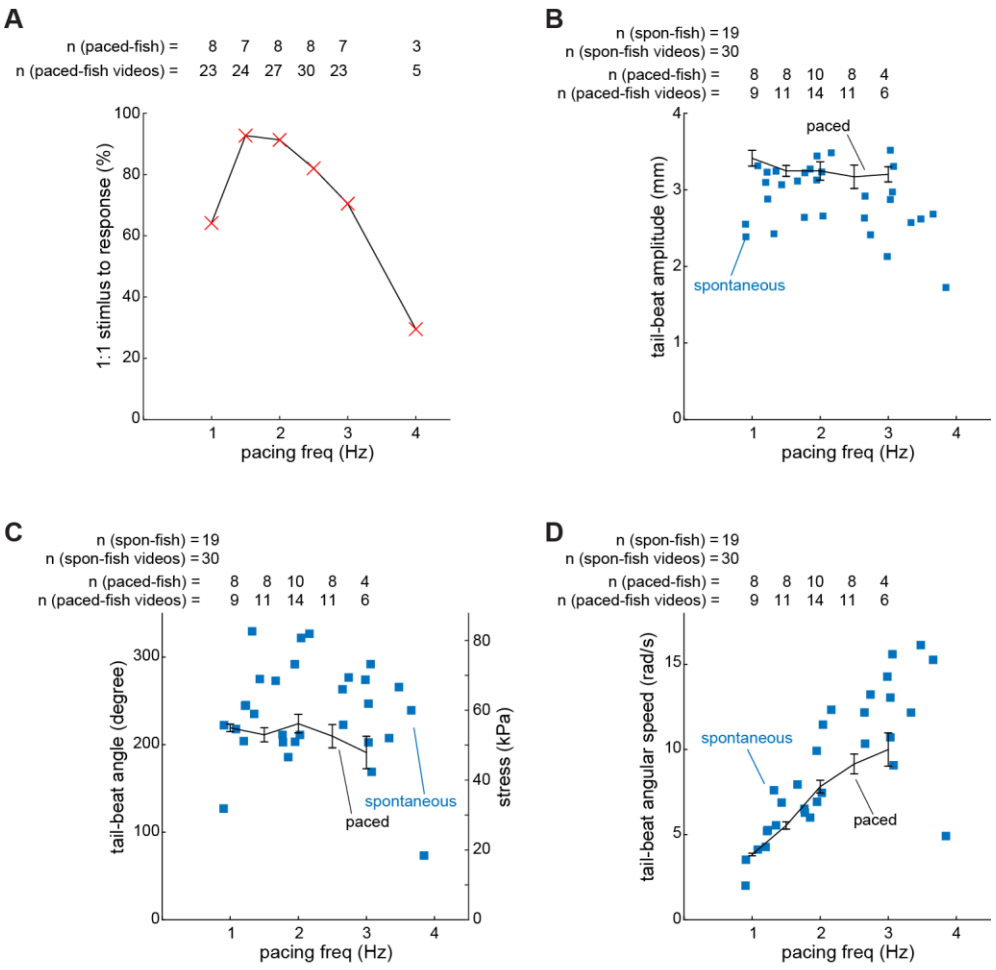

Fig. S9.

Body kinematics of biohybrid fish swimming under external optogenetic control (solid black line) and internal self-pacing (blue square marker). (A) 1: 1 stimulus-response of optogenetically paced biohybrid fish. The "1:1 stimulus to response" was quantified by measuring the response percentage of tissues contracting to each optical stimuli input. (B) Tail oscillation amplitude. (C) Tail beat angle. (D) Tail beat angular speed. Biohybrid fish maintain both tail oscillation amplitude and tail beat angle even at high pacing frequencies (3 to 4 Hz). Thus, an increase in the pacing frequency led to an increase in the tail beat angular speed of both external optogenetic controlled and autonomously swimming biohybrid fish, which improve their swimming speed. (n = 30 videos from 19 spontaneously paced fish and 54 videos from 12 optogenetically paced fish; data represent mean ± SEM).

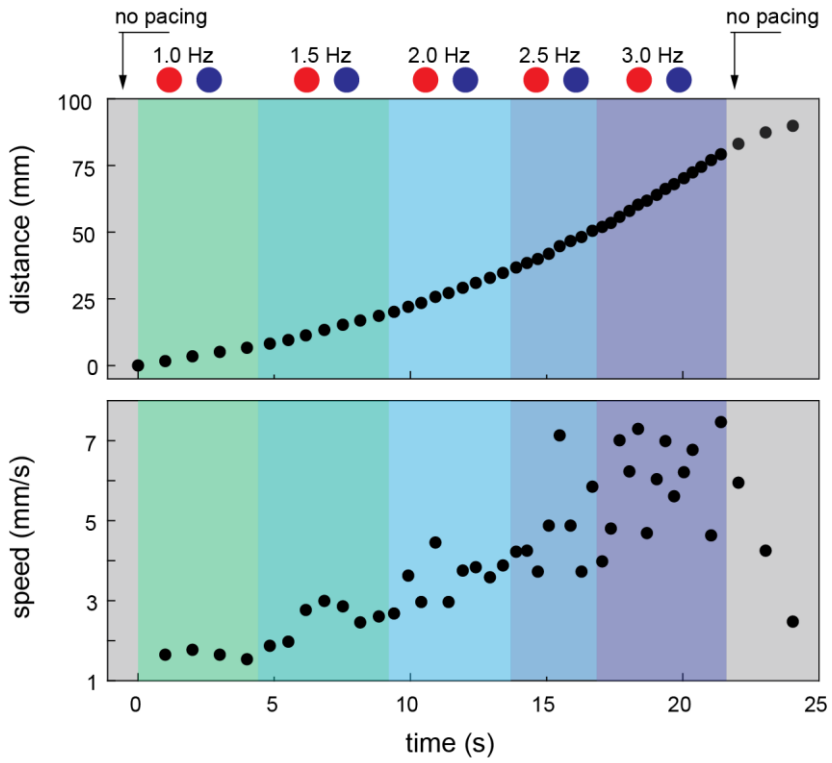

Fig. S10.

NRVM-based biohybrid fish accelerating speed by increasing pacing frequency. The NRVM-based biohybrid fish was stimulated with optical pacing with varying pacing frequencies (1, 1.5, 2, 2.5 and 3 Hz). Blue and red light independently activate ChR2- and ChrimsonR-expressed muscle layer, respectively, with 180 degree-phase shifts between red and blue lights. The data were acquired by video tracking of movie S8. The data are representative of independent experiments of 6 rat fish with similar results.

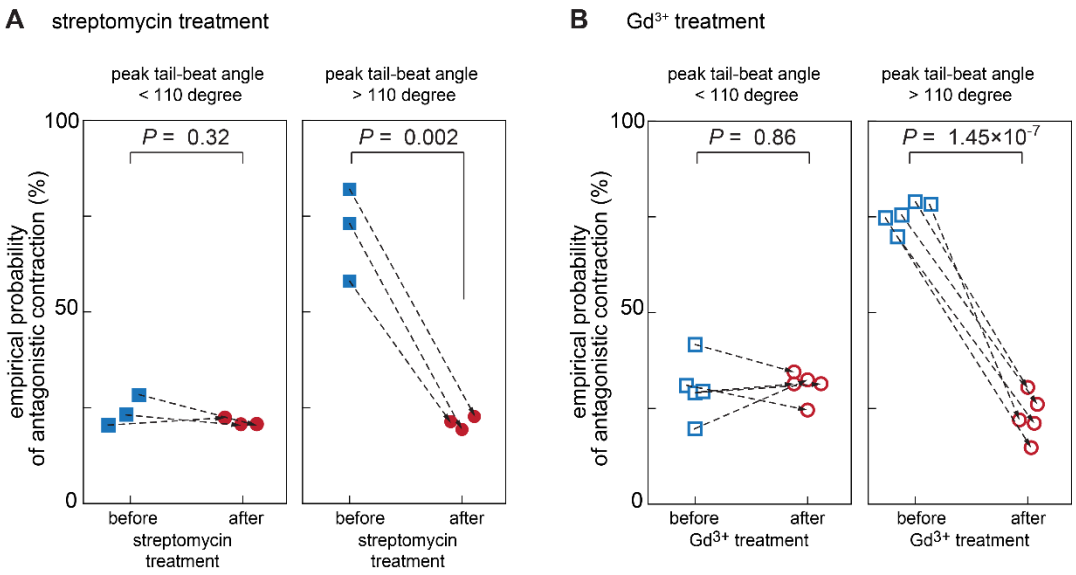

Fig. S11.

Disruption of antagonistic muscle contraction caused by the treatment of stretch-activated channel blockers, streptomycin (A) and Gd^{3+} (B). The larger tail-beat angle (> 110 degrees) induced antagonistic muscle contraction, but both stretch-activated ion channels inhibitors significantly decreased the empirical probability of antagonistic contractions in the biohybrid fish (Comparisons for all pairs using Tukey-Kramer Honest Significant Difference, n = 3 streptomycin-treated fish; 5 Gd^{3+}-treated fish).

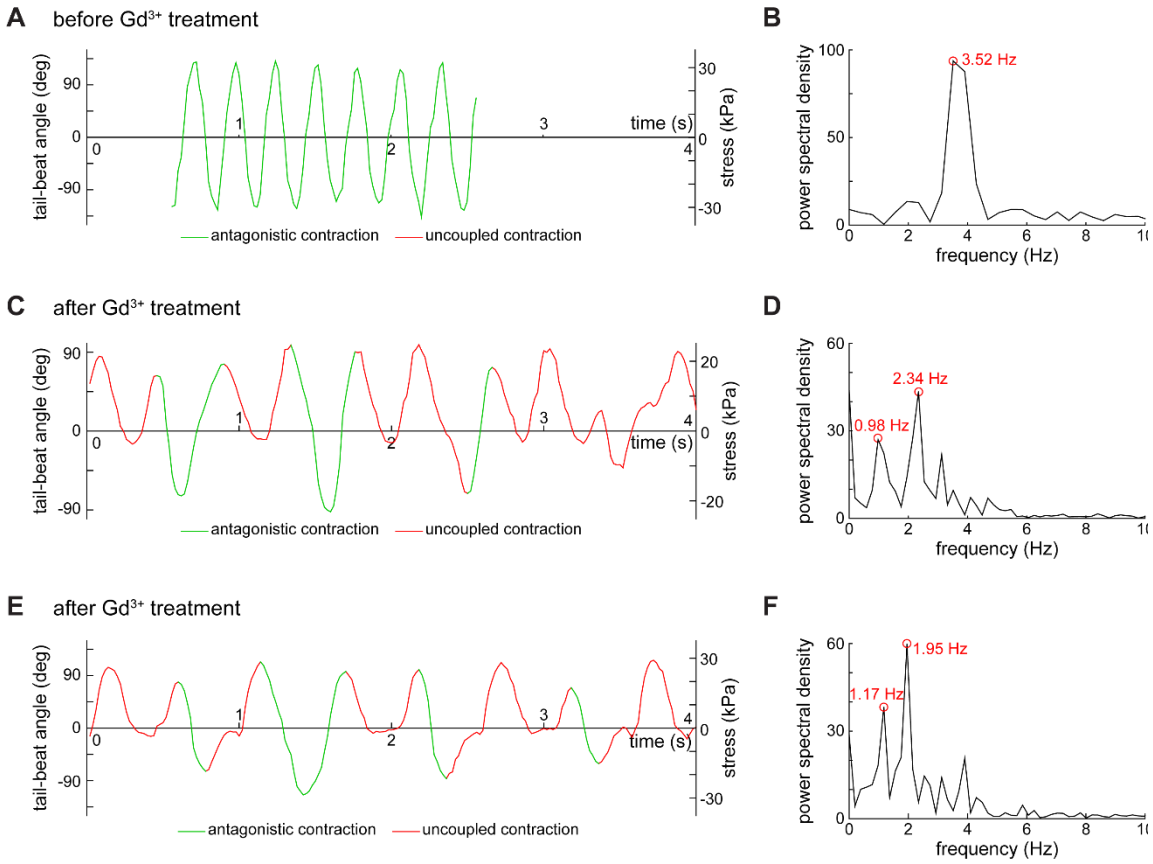

Fig. S12.

Body kinematics of biohybrid fish before and after Gd^{3+} treatment. (A and **B)** Tail-beat angle (A) and its frequency-domain analysis (power spectral density) (B) of hSC-CMs-based biohybrid fish before Gd^{3+} treatment. **(C** and **D)** Tail-beat angle (C) and its frequency-domain analysis (D) of the same biohybrid fish of (A and B) after Gd^{3+} treatment. **(E** and **F)** Tail-beat angle (E) and its frequency-domain analysis (F) of another hSC-CMs-based biohybrid fish after Gd^{3+} treatment. Before the inhibition of stretch-activated ion channels (Gd^{3+}), the left and right muscle tissues were antagonistically contracting with the same pacing frequency (3.52 Hz in B). But the Gd^{3+} treatment disrupted antagonistic contraction of muscular bilayer tissues: the left and right muscle tissues were independently contracting with two different pacing frequencies (2.34 and 0.98 Hz in D, and 1.95 and 1.17 Hz in F). Their frequencies are not harmonic, demonstrating the decoupling of spontaneous activities between muscular bilayer tissues. The tail-beat angles in A and B and C to F were calculated by video tracking of the body midlines of biohybrid fish in movies S11 and S12, respectively. The images are representative of three independent experiments.

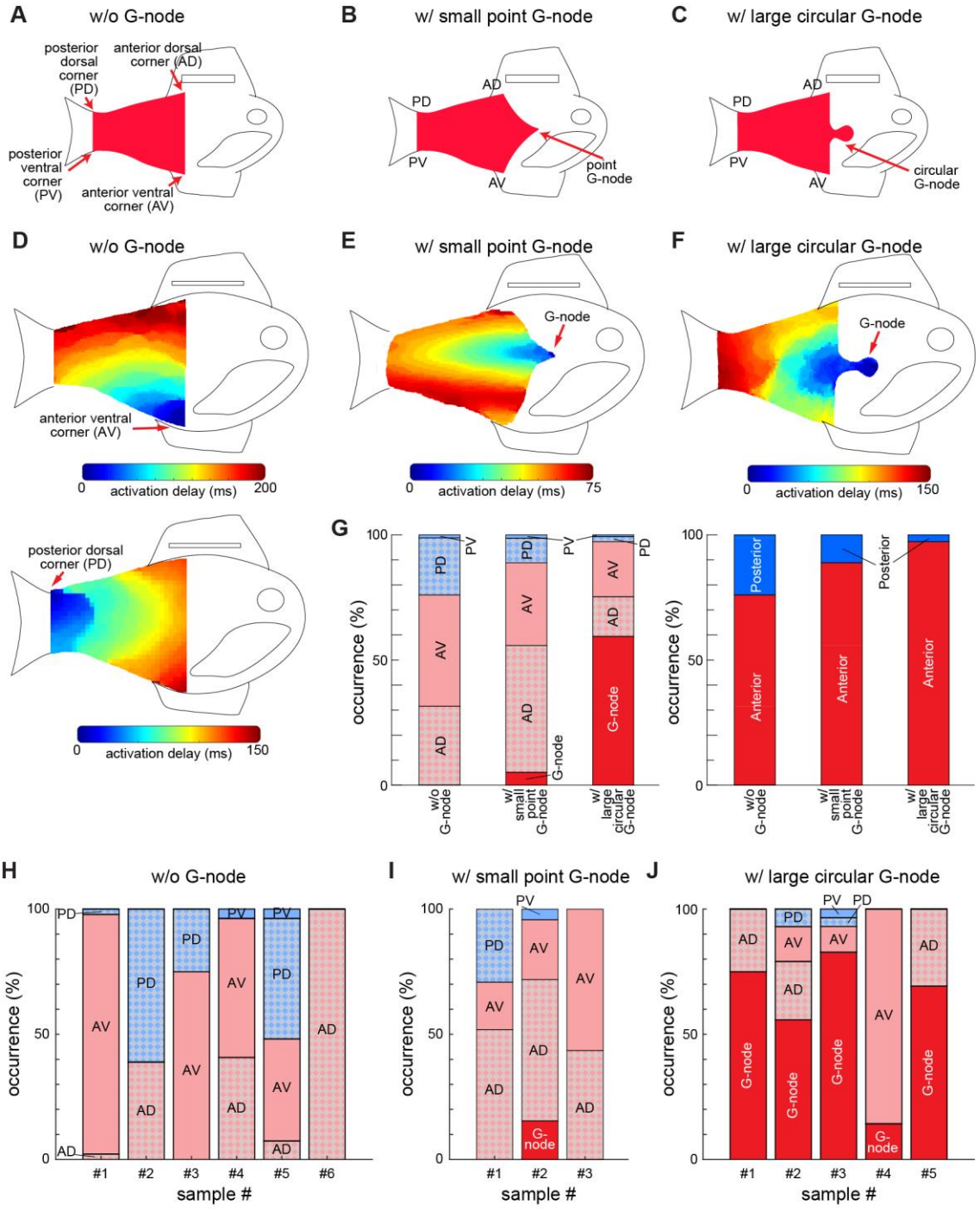

Fig. S13.

G-node. (A to **C)** The CMs in the four corners of the muscle tissue (A) and G-node (B: small point node design, and C: large circular node design) are geometrically isolated and surrounded with relatively small number of CMs. **(D** to **F)** Activation pattern initiated from anterior ventral corner (D top), posterior dorsal corner (D bottom) in tissues without G-node, and G-node in

tissue with G-node (E: small point node design and F: large circular node design). The data in (D) to (F) were acquired by video tracking of movie S15, respectively. **(G** to **J)** Probability of muscle activation sites in biohybrid fish: overall comparison (G) and individual sample results without G-node (n = 6 fish) (H) and with G-node (I: small point node design: n=3 fish, J: large circular node design: n = 5 fish). G-node, competing with the other four corners of the muscle tissue, predominantly initiated the sequential activation waves in the tissues equipped with large circular node design. The activation waves were predominantly initiated from the anterior having corners with acute angles, and the probability of muscle activation sites from anterior sides increased up to 97% by the G-node integration. The images are representative of independent experiments.

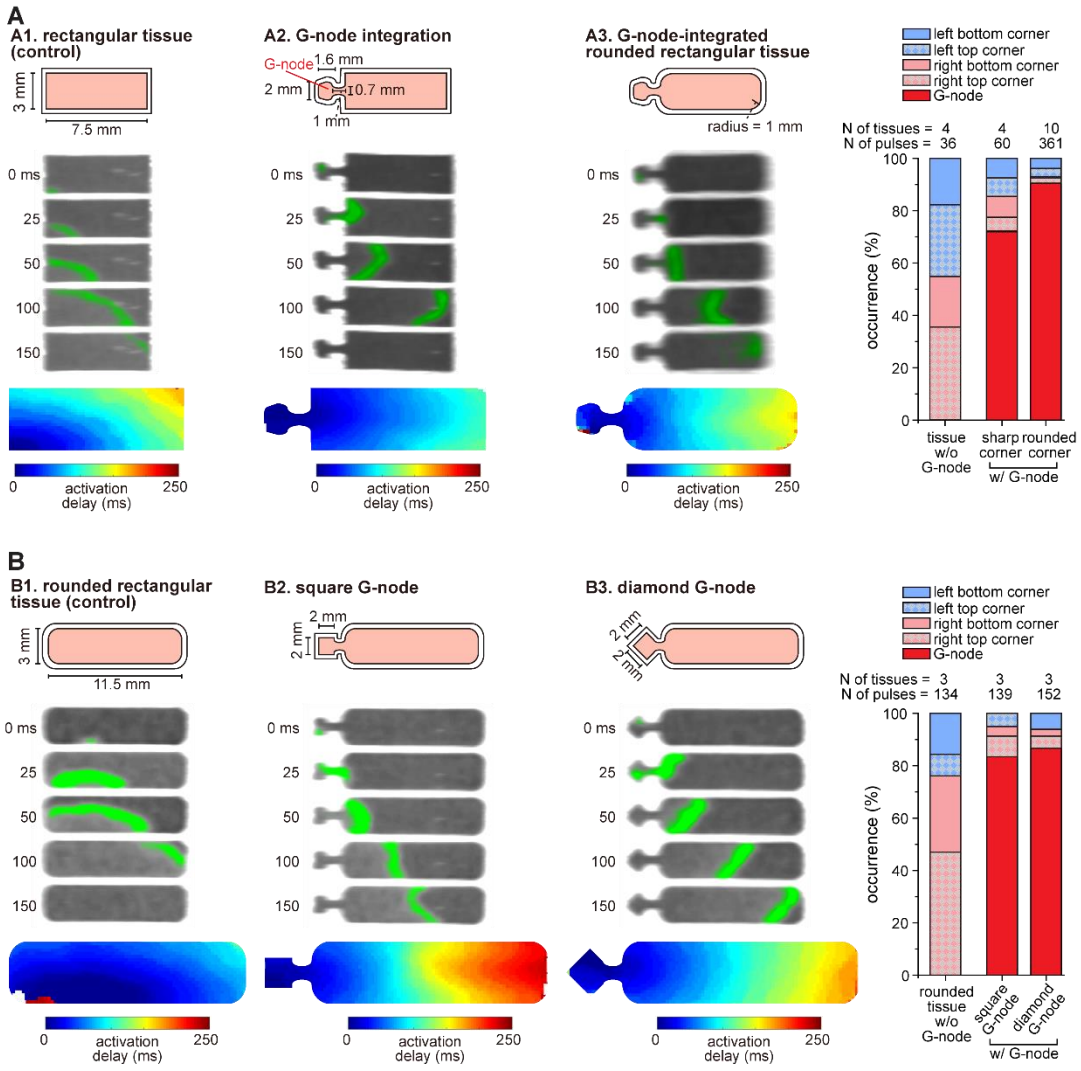

Fig. S14.

Muscle activation in G-node-integrated tissues. Design (top), Ca^{2+} propagation signals (middle), and activation map (bottom) (A) G-node integration in rectangular tissue with sharp and rounded corners. G-nodes integrated into a rectangular tissue predominantly activated the muscle construct compared to the four corners of the muscle tissue. Furthermore, the rounded corner decreased the empirical probability of initial activation at the corner, and thus the activation probability of the integrated G-node in the rounded tissue increased to 91%. (**B**) Different shapes of G-node in rounded rectangular tissue. The square and diamond G-nodes have a similar probability of activation at the G-node to the circular design (83 and 87% vs. 91%). This indicates that an acute angles in the small source tissue like the G-node is not critical in determining the activation site. Rather, it is the fewer number of cells in the smaller G-node tissue that acts as a source to initiate muscle activation.

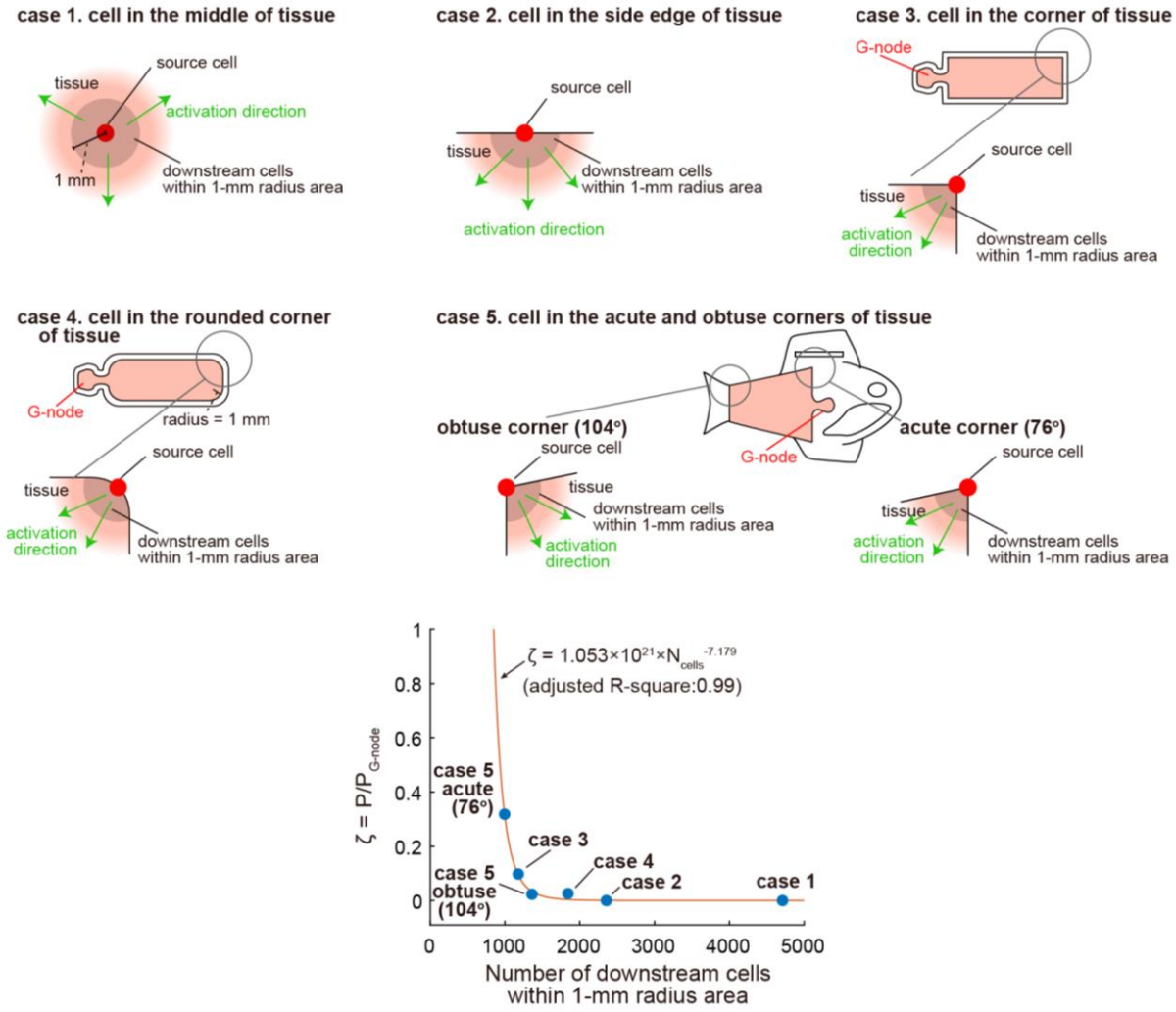

Fig. S15.

The contribution of the corner designs in the rectangular tissue to the probability of initial activation at the corner. The reduced sink load caused by the decreased number of downstream cells increases ζ (the probability of initial activation at the corner compared to the probability at the G-node) (18). For example, a rounded corner increases the number of downstream cells by 56% compared to a 90 degree shape corner, and decreases ζ by 73%, while the acute corner of our biohybrid fish body decreases the number of downstream cells by 16% compared to a 90 degree shape corner, thus increasing ζ by 220%. These results confirmed the source-sink mismatch principle that affects the initial muscle activation site. These experimental results and fitting plot can be used to guide future designs for the development of autonomously actuating cardiac muscle systems.

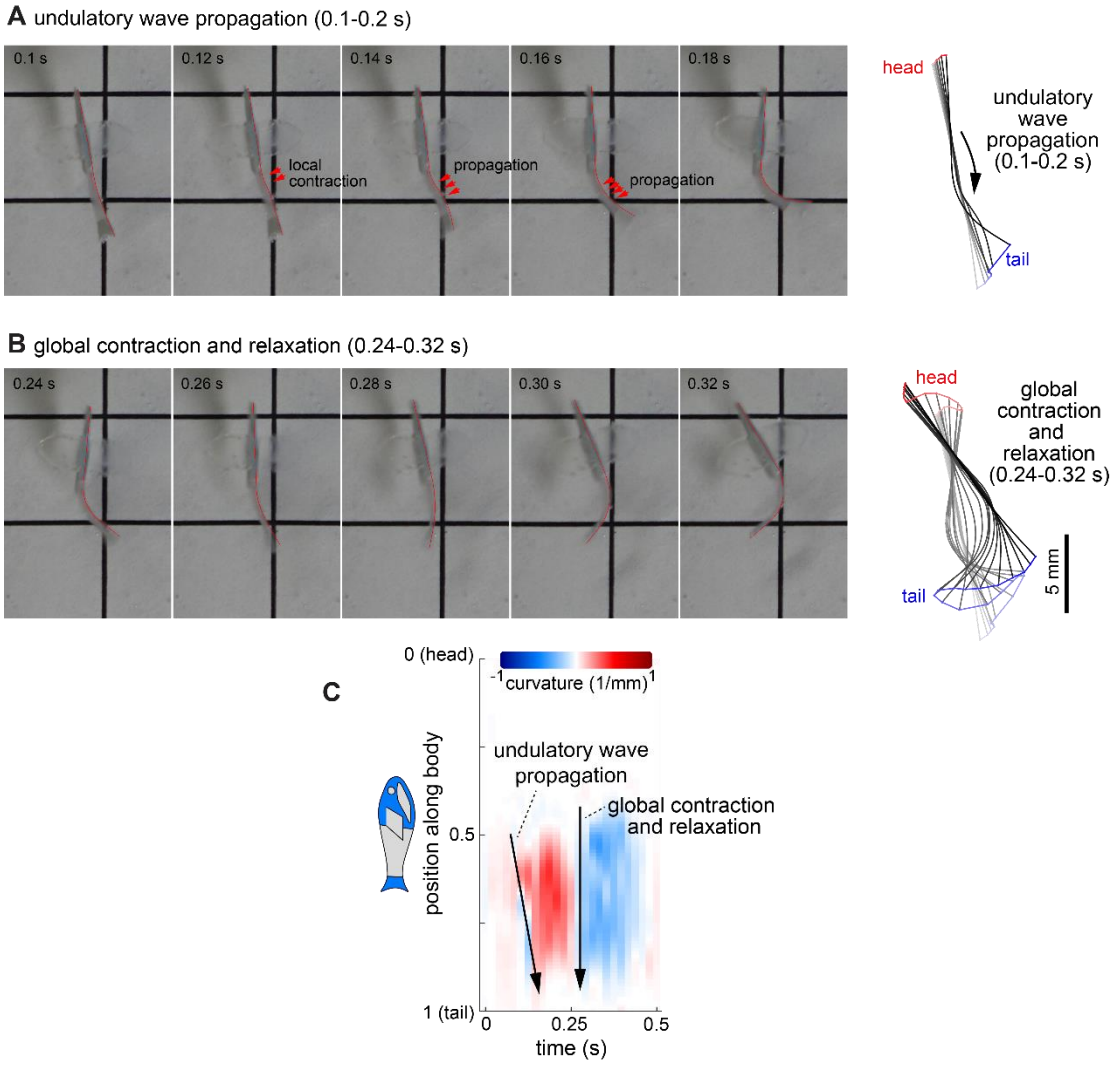

Fig. S16.

Change in midline kinematics during the swimming mode shift from undulatory wave propagation (0.1 to 0.2 s) to global muscle contraction (0.24 to 0.32 s). (A and **B)** Representative time lapse images and midline kinematics of biohybrid fish swimming via undulatory locomotion (A) and oscillatory locomotion (B). **(C)** Midline curvature. Biohybrid fish accelerating from rest induced sequential local muscle activation and contraction, leading to undulatory locomotion, while in subsequent muscle contractions, the biohybrid fish predominantly exhibited simultaneous global contractions and as a result, oscillatory locomotion with minimal body wave propagations. The midline curvatures were calculated by video tracking of the body midlines of biohybrid fish in movie S16.

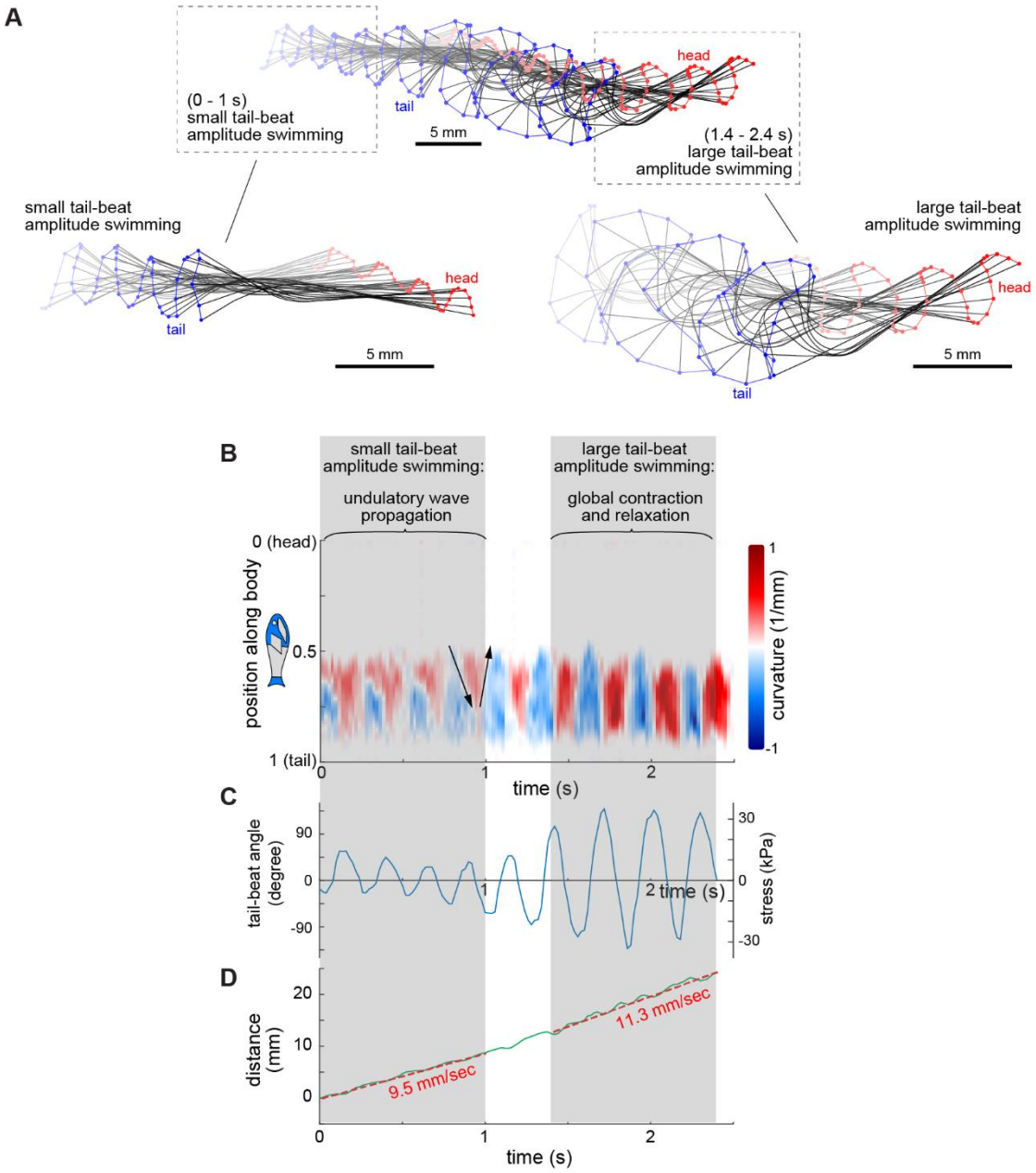

Fig. S17.

Change in midline kinematics (A) and midline curvature (B) of biohybrid fish during the shift from small oscillation amplitude swimming (0 to 1 s) to large oscillation amplitude swimming (1.4 to 2.4 s). The midline curvatures were calculated by video tracking of the body midlines of biohybrid fish in movie S22.

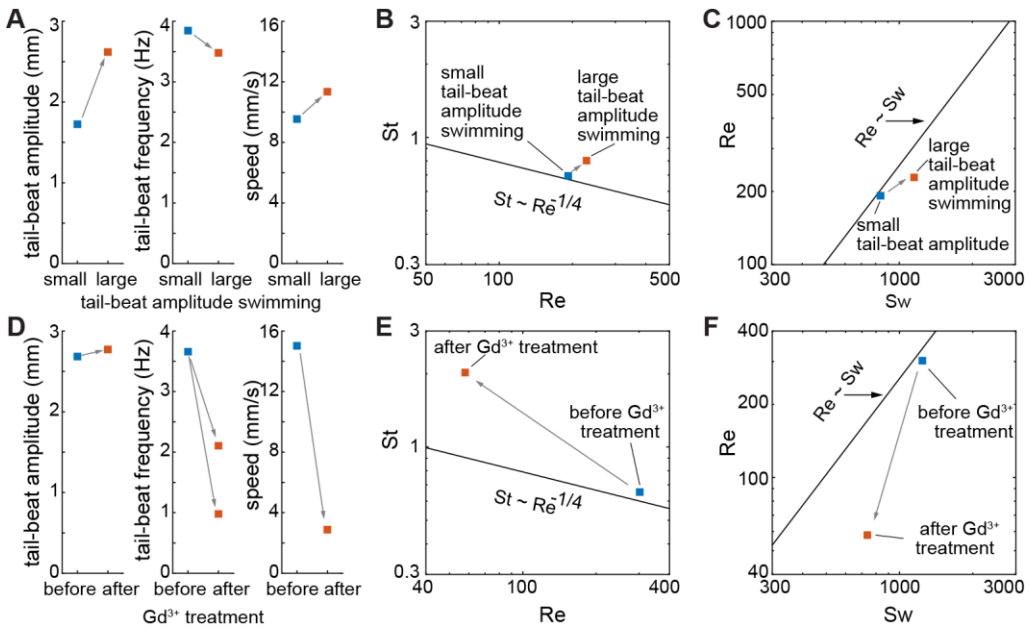

Fig. S18.

Comparison of swimming performance between the biohybrid fish before and after high tail-beat oscillation (A to C) and before and after the treatment of a stretch activated ion channel blocker, Gd^{3+} (D to F).

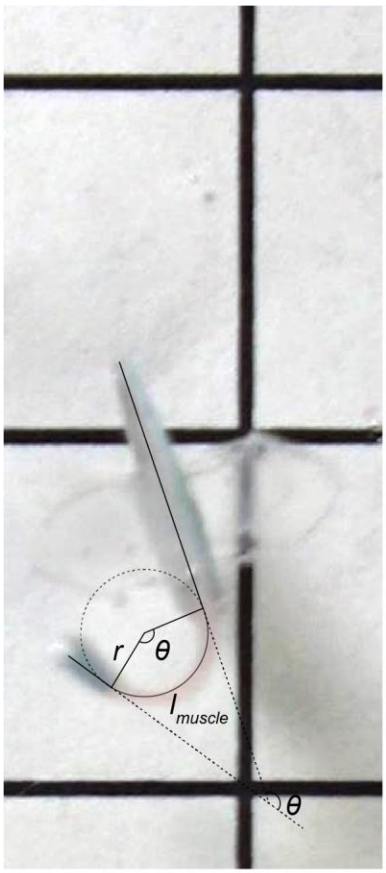

$$\kappa = \frac{1}{r} = \frac{\theta}{l_{muscle}}$$

Fig. S19.

Geometric relationship of the curvature (κ), radius of curvature (r), length of muscle tissue (l_{muscle}), and tail-beat angle (θ) ($\kappa = 1/r = \theta / l_{muscle}$)

References and Notes

1. S. Vogel, *Vital Circuits: On Pumps, Pipes, and the Workings of Circulatory Systems* (Oxford Univ. Press, 1992).

2. J. C. Nawroth, H. Lee, A. W. Feinberg, C. M. Ripplinger, M. L. McCain, A. Grosberg, J. O. Dabiri, K. K. Parker, A tissue-engineered jellyfish with biomimetic propulsion. *Nat. Biotechnol.* **30**, 792–797 (2012). doi:10.1038/nbt.2269 Medline

3. S. J. Park, M. Gazzola, K. S. Park, S. Park, V. Di Santo, E. L. Blevins, J. U. Lind, P. H. Campbell, S. Dauth, A. K. Capulli, F. S. Pasqualini, S. Ahn, A. Cho, H. Yuan, B. M. Maoz, R. Vijaykumar, J.-W. Choi, K. Deisseroth, G. V. Lauder, L. Mahadevan, K. K. Parker, Phototactic guidance of a tissue-engineered soft-robotic ray. *Science* **353**, 158–162 (2016). doi:10.1126/science.aaf4292 Medline

4. L. Ricotti, B. Trimmer, A. W. Feinberg, R. Raman, K. K. Parker, R. Bashir, M. Sitti, S. Martel, P. Dario, A. Menciassi, Biohybrid actuators for robotics: A review of devices actuated by living cells. *Sci. Robot.* **2**, eaaq0495 (2017). doi:10.1126/scirobotics.aaq0495 Medline

5. H. E. ter Keurs, Electromechanical coupling in the cardiac myocyte; stretch-arrhythmia feedback. *Pflugers Arch.* **462**, 165–175 (2011). doi:10.1007/s00424-011-0944-3 Medline

6. T. A. Quinn, P. Kohl, Cardiac Mechano-Electric Coupling: Acute Effects of Mechanical Stimulation on Heart Rate and Rhythm. *Physiol. Rev.* **101**, 37–92 (2021). doi:10.1152/physrev.00036.2019 Medline

7. T. A. Quinn, P. Kohl, U. Ravens, Cardiac mechano-electric coupling research: Fifty years of progress and scientific innovation. *Prog. Biophys. Mol. Biol.* **115**, 71–75 (2014). doi:10.1016/j.pbiomolbio.2014.06.007 Medline

8. B. E. Dabiri, H. Lee, K. K. Parker, A potential role for integrin signaling in mechanoelectrical feedback. *Prog. Biophys. Mol. Biol.* **110**, 196–203 (2012). doi:10.1016/j.pbiomolbio.2012.07.002 Medline

9. O. Friedrich, S. Wagner, A. R. Battle, S. Schürmann, B. Martinac, Mechano-regulation of the beating heart at the cellular level—Mechanosensitive channels in normal and diseased heart. *Prog. Biophys. Mol. Biol.* **110**, 226–238 (2012). doi:10.1016/j.pbiomolbio.2012.08.009 Medline

10. T. A. Quinn, H. Jin, P. Lee, P. Kohl, Mechanically Induced Ectopy via Stretch-Activated Cation-Nonselective Channels Is Caused by Local Tissue Deformation and Results in Ventricular Fibrillation if Triggered on the Repolarization Wave Edge (Commotio Cordis). *Circ. Arrhythm. Electrophysiol.* **10**, e004777 (2017). doi:10.1161/CIRCEP.116.004777 Medline

11. S. D. Unudurthi, R. M. Wolf, T. J. Hund, Role of sinoatrial node architecture in maintaining a balanced source-sink relationship and synchronous cardiac pacemaking. *Front. Physiol.* **5**, 446 (2014). doi:10.3389/fphys.2014.00446 Medline

12. A. G. Kléber, Y. Rudy, Basic mechanisms of cardiac impulse propagation and associated arrhythmias. *Physiol. Rev.* **84**, 431–488 (2004). doi:10.1152/physrev.00025.2003 Medline

13. S. Rohr, J. P. Kucera, V. G. Fast, A. G. Kléber, Paradoxical improvement of impulse conduction in cardiac tissue by partial cellular uncoupling. *Science* **275**, 841–844 (1997). doi:10.1126/science.275.5301.841 Medline

14. B. Bullard, A. Pastore, Regulating the contraction of insect flight muscle. *J. Muscle Res. Cell Motil.* **32**, 303–313 (2011). doi:10.1007/s10974-011-9278-1 Medline

15. R. W. Joyner, F. J. van Capelle, Propagation through electrically coupled cells. How a small SA node drives a large atrium. *Biophys. J.* **50**, 1157–1164 (1986). doi:10.1016/S0006-3495(86)83559-7 Medline

16. Materials and methods are available as supplementary materials.

17. S. J. Park, D. Zhang, Y. Qi, Y. Li, K. Y. Lee, V. J. Bezzerides, P. Yang, S. Xia, S. L. Kim, X. Liu, F. Lu, F. S. Pasqualini, P. H. Campbell, J. Geva, A. E. Roberts, A. G. Kleber, D. J. Abrams, W. T. Pu, K. K. Parker, Insights Into the Pathogenesis of Catecholaminergic Polymorphic Ventricular Tachycardia From Engineered Human Heart Tissue. *Circulation* **140**, 390–404 (2019). doi:10.1161/CIRCULATIONAHA.119.039711 Medline

18. M. L. McCain, A. Agarwal, H. W. Nesmith, A. P. Nesmith, K. K. Parker, Micromolded gelatin hydrogels for extended culture of engineered cardiac tissues. *Biomaterials* **35**, 5462–5471 (2014). doi:10.1016/j.biomaterials.2014.03.052 Medline

19. E. S. Boyden, F. Zhang, E. Bamberg, G. Nagel, K. Deisseroth, Millisecond-timescale, genetically targeted optical control of neural activity. *Nat. Neurosci.* **8**, 1263–1268 (2005). doi:10.1038/nn1525 Medline

20. N. C. Klapoetke, Y. Murata, S. S. Kim, S. R. Pulver, A. Birdsey-Benson, Y. K. Cho, T. K. Morimoto, A. S. Chuong, E. J. Carpenter, Z. Tian, J. Wang, Y. Xie, Z. Yan, Y. Zhang, B. Y. Chow, B. Surek, M. Melkonian, V. Jayaraman, M. Constantine-Paton, G. K.-S. Wong, E. S. Boyden, Independent optical excitation of distinct neural populations. *Nat. Methods* **11**, 338–346 (2014). doi:10.1038/nmeth.2836 Medline

21. F. Gannier, E. White, A. Lacampagne, D. Garnier, J. Y. Le Guennec, Streptomycin reverses a large stretch induced increases in [Ca2+]i in isolated guinea pig ventricular myocytes. *Cardiovasc. Res.* **28**, 1193–1198 (1994). doi:10.1093/cvr/28.8.1193 Medline

22. X. C. Yang, F. Sachs, Block of stretch-activated ion channels in Xenopus oocytes by gadolinium and calcium ions. *Science* **243**, 1068–1071 (1989). doi:10.1126/science.2466333 Medline

23. A. G. Kléber, Q. Jin, Coupling between cardiac cells-An important determinant of electrical impulse propagation and arrhythmogenesis. *Biophys. Rev.* **2**, 031301 (2021). doi:10.1063/5.0050192 Medline

24. K. Y. Lee, S. J. Park, Optical stimulation for independent activation of muscles: Matlab and Labview, Zenodo (2021); doi:10.5281/zenodo.5618323.

25. A. W. Feinberg, A. Feigel, S. S. Shevkoplyas, S. Sheehy, G. M. Whitesides, K. K. Parker, Muscular thin films for building actuators and powering devices. *Science* **317**, 1366–1370 (2007). doi:10.1126/science.1146885 Medline

26. J. Xi, J. J. Schmidt, C. D. Montemagno, Self-assembled microdevices driven by muscle. *Nat. Mater.* **4**, 180–184 (2005). doi:10.1038/nmat1308 Medline

27. C. Cvetkovic, R. Raman, V. Chan, B. J. Williams, M. Tolish, P. Bajaj, M. S. Sakar, H. H. Asada, M. T. A. Saif, R. Bashir, Three-dimensionally printed biological machines powered by skeletal muscle. *Proc. Natl. Acad. Sci. U.S.A.* **111**, 10125–10130 (2014). doi:10.1073/pnas.1401577111 Medline

28. V. Chan, K. Park, M. B. Collens, H. Kong, T. A. Saif, R. Bashir, Development of miniaturized walking biological machines. *Sci. Rep.* **2**, 857 (2012). doi:10.1038/srep00857 Medline

29. J. Kim, J. Park, S. Yang, J. Baek, B. Kim, S. H. Lee, E.-S. Yoon, K. Chun, S. Park, Establishment of a fabrication method for a long-term actuated hybrid cell robot. *Lab Chip* **7**, 1504–1508 (2007). doi:10.1039/b705367c Medline

30. Y. Akiyama, T. Hoshino, K. Iwabuchi, K. Morishima, Room temperature operable autonomously moving bio-microrobot powered by insect dorsal vessel tissue. *PLOS ONE* **7**, e38274 (2012). doi:10.1371/journal.pone.0038274 Medline

31. Y. Akiyama, K. Odaira, K. Sakiyama, T. Hoshino, K. Iwabuchi, K. Morishima, Rapidly-moving insect muscle-powered microrobot and its chemical acceleration. *Biomed. Microdevices* **14**, 979–986 (2012). doi:10.1007/s10544-012-9700-5 Medline

32. G. J. Pagan-Diaz, X. Zhang, L. Grant, Y. Kim, O. Aydin, C. Cvetkovic, E. Ko, E. Solomon, J. Hollis, H. Kong, T. Saif, M. Gazzola, R. Bashir, Simulation and Fabrication of Stronger, Larger, and Faster Walking Biohybrid Machines. *Adv. Funct. Mater.* **28**, 1801145 (2018). doi:10.1002/adfm.201801145

33. R. Raman, C. Cvetkovic, S. G. M. Uzel, R. J. Platt, P. Sengupta, R. D. Kamm, R. Bashir, Optogenetic skeletal muscle-powered adaptive biological machines. *Proc. Natl. Acad. Sci. U.S.A.* **113**, 3497–3502 (2016). doi:10.1073/pnas.1516139113 Medline

34. B. J. Williams, S. V. Anand, J. Rajagopalan, M. T. Saif, A self-propelled biohybrid swimmer at low Reynolds number. *Nat. Commun.* **5**, 3081 (2014). doi:10.1038/ncomms4081 Medline

35. O. Aydin, X. Zhang, S. Nuethong, G. J. Pagan-Diaz, R. Bashir, M. Gazzola, M. T. A. Saif, Neuromuscular actuation of biohybrid motile bots. *Proc. Natl. Acad. Sci. U.S.A.* **116**, 19841–19847 (2019). doi:10.1073/pnas.1907051116 Medline

36. G. K. Taylor, R. L. Nudds, A. L. Thomas, Flying and swimming animals cruise at a Strouhal number tuned for high power efficiency. *Nature* **425**, 707–711 (2003). doi:10.1038/nature02000 Medline

37. M. Gazzola, M. Argentina, L. Mahadevan, Scaling macroscopic aquatic locomotion. *Nat. Phys.* **10**, 758–761 (2014). doi:10.1038/nphys3078

38. H. E. Jackson, P. W. Ingham, Control of muscle fibre-type diversity during embryonic development: The zebrafish paradigm. *Mech. Dev.* **130**, 447–457 (2013). doi:10.1016/j.mod.2013.06.001 Medline

39. T. N. Wise, M. A. B. Schwalbe, E. D. Tytell, Hydrodynamics of linear acceleration in bluegill sunfish, *Lepomis macrochirus*. *J. Exp. Biol.* **221**, jeb.190892 (2018). doi:10.1242/jeb.190892 Medline

40. Y. Morimoto, H. Onoe, S. Takeuchi, Biohybrid robot powered by an antagonistic pair of skeletal muscle tissues. *Sci. Robot.* **3**, eaat4440 (2018). doi:10.1126/scirobotics.aat4440 Medline

41. R. Du, Z. Li, K. Youcef-Toumi, P. Valdivia y Alvarado, in *Robot Fish: Bio-inspired Fishlike Underwater Robots*, R. Du, Z. Li, K. Youcef-Toumi, P. Valdivia y Alvarado, Eds. (Springer, 2015), pp. 1–24.

42. G. V. Lauder, J. L. Tangorra, in *Robot Fish: Bio-inspired Fishlike Underwater Robots*, R. Du, Z. Li, K. Youcef-Toumi, P. Valdivia y Alvarado, Eds. (Springer, 2015), pp. 25–49.

43. T. Opthof, V. M. Meijborg, C. N. Belterman, R. Coronel, Synchronization of repolarization by mechano-electrical coupling in the porcine heart. *Cardiovasc. Res.* **108**, 181–187 (2015). doi:10.1093/cvr/cvv140 Medline

44. T. A. Quinn, Cardiac mechano-electric coupling: A role in regulating normal function of the heart? *Cardiovasc. Res.* **108**, 1–3 (2015). doi:10.1093/cvr/cvv203 Medline

45. J. Almendral, R. Caulier-Cisterna, J. L. Rojo-Álvarez, Resetting and entrainment of reentrant arrhythmias: part I: concepts, recognition, and protocol for evaluation: surface ECG versus intracardiac recordings. *Pacing Clin. Electrophysiol.* **36**, 508–532 (2013). doi:10.1111/pace.12064 Medline

46. W. Thielicke, E. J. Stamhuis, PIVlab – Towards User-friendly, Affordable and Accurate Digital Particle Image Velocimetry in MATLAB. *J. Open Res. Softw.* **2**, e30 (2014). doi:10.5334/jors.bl

47. W. Liang, P. Han, E. H. Kim, J. Mak, R. Zhang, A. G. Torrente, J. I. Goldhaber, E. Marbán, H. C. Cho, Canonical Wnt signaling promotes pacemaker cell specification of cardiac mesodermal cells derived from mouse and human embryonic stem cells. *Stem Cells* **38**, 352–368 (2020). doi:10.1002/stem.3106 Medline

48. V. A. Maltsev, E. G. Lakatta, Normal heart rhythm is initiated and regulated by an intracellular calcium clock within pacemaker cells. *Heart Lung Circ.* **16**, 335–348 (2007). doi:10.1016/j.hlc.2007.07.005 Medline